



Temperature-controlled spatiotemporally modulated phononic crystal for achieving nonreciprocal acoustic wave propagation

Justin Palacios, ¹ Lazaro Calderin, ¹ Allan Chon, ¹ Ian Frankel, ² Jihad Alqasimi, ³ Florian Allein, ² Rachel Gorelik, ¹ Trevor Lata, ¹ Richard Curradi, ¹ Gabrielle Lambert-Milak, ¹ Anuja Oke, ¹ Neale Smith, ¹ Maroun Abi Ghanem, ² Pierre Lucas, ¹ Di Nicholas Boechler, ², and Pierre Deymier ¹ D

ABSTRACT:

We computationally investigate a method for spatiotemporally modulating a material's elastic properties, leveraging thermal dependence of elastic moduli, with the goal of inducing nonreciprocal propagation of acoustic waves. Acoustic wave propagation in an aluminum thin film subjected to spatiotemporal boundary heating from one side and constant cooling from the other side was simulated via the finite element method. Material property modulation patterns induced by the asymmetric boundary heating are found to be non-homogenous with depth. Despite these inhomogeneities, it will be shown that such thermoelasticity can still be used to achieve nonreciprocal acoustic wave propagation. © 2022 Acoustical Society of America. https://doi.org/10.1121/10.0011543

(Received 24 January 2021; revised 11 May 2022; accepted 13 May 2022; published online 2 June 2022)

[Editor: Badreddine Assouar] Pages: 3669–3675

I. INTRODUCTION

Periodic modulation of a material's properties in space and time has been shown to enable one-way wave propagation. 1-12 For acoustic and elastic waves, this process can be thought of as one that creates a phononic crystal that supports bandgaps and then moves the crystal with some velocity relative to a propagating wave. Compared to a static phononic crystal, the added time modulation breaks the symmetry of the band structure around the Brillouin zone (BZ) center such that the bandgaps for positive and negative wavevectors occur in different frequency ranges. As a result of this asymmetry and in contrast to wave propagation in conventional materials, waves with a given frequency propagate nonreciprocally and they do not propagate equally when traveling in one direction compared to the opposite direction. 13 Systems supporting such nonreciprocal wave propagation have been proposed for applications such as zero backscatter waveguides and logic devices.

Methods shown to experimentally induce nonreciprocal acoustic wave propagation via spatiotemporal modulation have leveraged various forms of electromagnetic-elastic coupling. 8-11,14 In this paper, using finite element method (FEM) simulations, we show how spatiotemporal elastic property modulation via the thermal dependence of elastic moduli can be used to enable nonreciprocal elastic wave propagation in metallic thin films (we note a related study exploring modified diffusive heat flux in the presence of

spatiotemporally modulated thermal conductivity and heat capacity¹⁵). This method has potential benefits, including its applicability to a wide range of materials, as well as potential flexibility of unit cell size and modulation speed via future photo- or electrothermal heating schemes. One major drawback, as shown herein, is that this method results in a nonuniform elastic modulus profile throughout the depth of the film. However, despite this disadvantage, we also show that such nonuniformity does not preclude the breaking of acoustic wave propagation symmetry.

II. MATERIALS AND METHODS

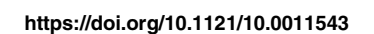
Aluminum films subjected to dynamic mechanical and thermal loads were simulated using the time-dependent twodimensional (2D) heat transfer and solid mechanics modules within the COMSOL Multiphysics[®] FEM software (version 5.4; COMSOL AB, Stockholm, Sweden). The simulations simultaneously solve the thermal and elastic equations, with the thermoelastic equation of aluminum's temperaturedependent Young's modulus coupling the two models. The setup is illustrated in Fig. 1(a), where the y axis denotes the "out-of-plane" direction, the x axis denotes the "in-plane" direction, and the z-axis denotes the "depth" direction. Film thicknesses (in the out-of-plane direction) of 1, 0.5, and $0.25 \,\mu\mathrm{m}$ were studied. The depth of the film was $z = 1 \,\mathrm{mm}$, and plane strain behavior was assumed for this direction. Rectangular elements of length 1 μ m \times 0.25 μ m were used. Mesh size independence studies were conducted to verify that 1 μ m \times 0.25 μ m is a sufficient element size, whereas for

¹Department of Materials Science and Engineering, The University of Arizona, 1235 James E. Rogers Way, Tucson, Arizona 85719, USA

²Department of Mechanical and Aerospace Engineering, University of California, San Diego, 9500 Gilman Drive MC 0411, La Jolla, California 92093, USA

³Mechanical Engineering Department, King Fahd University of Petroleum and Minerals, Academic Belt Road, Box 5069, Dhahran 31261. Saudi Arabia

a)Electronic mail: nboechler@eng.ucsd.edu





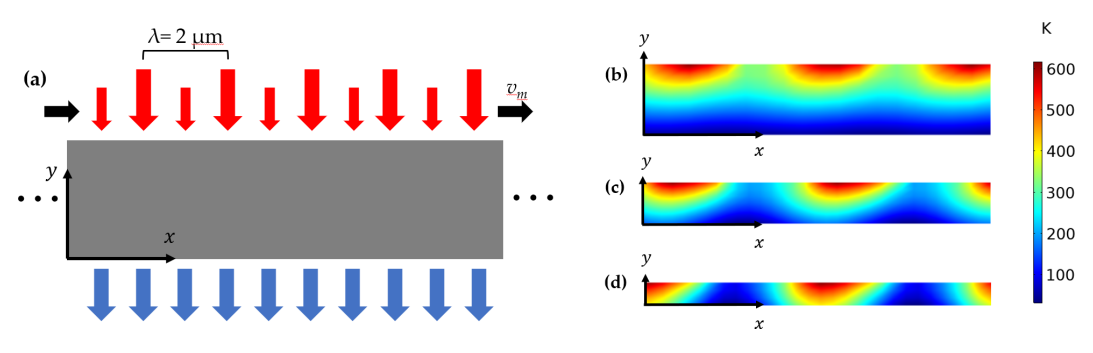


FIG. 1. (Color online) The (a) schematic of a metallic thin film subjected to a periodic heat flux along the top boundary with a $2 \mu m$ period and constant cooling rate along the bottom boundary is shown. The top heat flux pattern moves across the top boundary with a speed of $v_m = 300 \,\text{m/s}$. The $4 \,\mu m$ length sections show the thermal patterns formed in films of (b) $1 \,\mu m$, (c) $0.5 \,\mu m$, and (d) $0.25 \,\mu m$ thicknesses.

smaller elements, no change was observed in the simulated acoustic and thermal responses of the system. Quadratic elements are employed in this study. The ambient temperature was set to 300 K. The top boundary of the film was set as a boundary heat flux that introduces heat into the system in a periodic pattern, and the bottom boundary of the film was set as a constant cooling boundary heat flux. The top and bottom surfaces of the plate were set as mechanically "free" boundary conditions. The application of spatiotemporally varying heating only on one side of the film was chosen to model potential future experimental scenarios, leveraging optothermal heating strategies. For characterization of the acoustic dispersion of the films, the length of the film was set to $400 \,\mu\mathrm{m}$ with periodic boundary conditions, and an out-of-plane Gaussian impulse (with a standard deviation of 1 ns) point force was applied in the center of the film at the top and bottom surfaces in the same, out-of-plane direction. By exciting the two surfaces in the same direction, we more closely mimic the shape of and primarily excite antisymmetric (flexural) Lamb wave modes. In the experimental scenarios, leveraging laser-based techniques also for the acoustic excitation as well as the thermal modulation, we expect to primarily excite such antisymmetric modes caused by the strong optical absorption of aluminum. ¹⁶ For characterization of nonreciprocal acoustic wave transmission at single frequency excitations, two 200 µm long homogenous regions were added on either end of the $400 \, \mu \text{m}$ long patterned region in the film. Thermal periodic boundary conditions at the left and right ends were used for the characterization of the nonreciprocal behavior. The mostly vertical heat flow between the top and bottom surfaces of the film prevented significant temperature-induced alteration of the homogenous regions. Each film was then excited by a sinusoidal prescribed displacement, sequentially, at the left and right boundaries.

Aluminum was used as the material of choice because of its high thermal conductivity, $k_{\rm th}=238\,{\rm W/m}$ K, and thermal diffusivity, $\alpha=97\,{\rm mm^2/s},^{17}$ which helps maintain a uniform temperature profile throughout the thickness of the film. We assumed that the heat capacity, $C_p=900\,{\rm J/kg}$ K, and thermal conductivity are constant with the temperature. 17,18 The aluminum film was modeled with a density of $\rho=2700\,{\rm kg/m^3}$ and a Poisson's ratio of $\nu=0.33$. The temperature-dependent elastic modulus of the aluminum was modeled as

E(T) = A(T-300) + 70, where A = 0.0677 GPa/K and the film temperature, T, is in Kelvin. The Poisson ratio is kept constant for this simulation. From a temperature range of 0–1000 K, the Poisson ratio changes from 0.34 to 0.38, which is about a 10% increase. This is overshadowed by the greater than 40% increase we see in Young's modulus from 600 to 100 K. Similarly, the mass density for aluminum varies approximately between 2725 and 2625 kg/m³ in the temperature range under consideration, less than a 4% change, which is considered negligible for the purpose of this simulation. The property of the simulation.

The spatiotemporally periodic heating pattern applied the top boundary was modeled as q'' = Q(1)+sgn(sin $((2\pi/\lambda)x - 2\pi Ft))$), where $\lambda = 2 \mu m$ is the spatial period and $F = 150 \,\text{MHz}$ is the frequency of the heating pattern, resulting in a translation speed of the pattern of $v_m = 300 \,\mathrm{m/s}$, and sgn() denotes the signum function.²² The modulation frequency of the thermal pattern impacts the depth of penetration of the modulation. The penetration depth can be estimated as $d = \sqrt{k/\pi F C_p \rho}$, where, using the given material parameters and modulation frequency, $d = 0.46 \,\mu\text{m}$. From this, the ratio of penetration depth to film thickness, r_p , can be defined for each system. Values for r_p are reported as 0.456 for the 1 μ m film, 0.912 for the 0.5 μ m film, and 1.82 for the 0.25 μ m film. We neglect the thermal expansion effects in our simulation as we estimate their influence to be significantly smaller than that due to the change in elasticity. For instance, assuming a linear thermal expansion coefficient for aluminum of $\alpha_T = 23.6 \,\mu\text{m/m}$ K (Ref. 24) and isotropic volumetric expansion proportional to the cube of α_T , the density change per change in temperature is over 10 orders of magnitude smaller than the elastic modulus change. Furthermore, elastic wave generation at the modulation frequency is expected to be inefficient as the frequency and wavelength pair of the modulation does not match with the flexural mode dispersion relation. The factor, Q, was set to give a difference between the maximum and minimum temperature of 475 K in each of the films. The bottom boundary of the film is modeled as a heat flux boundary with a magnitude of -Q, ranging from 77.4 to 142.8 GW/m². Such heat flux values may be possible using forced cooling with liquid oxygen.²⁵ This keeps the film in thermal equilibrium and maintains the shape of the moving thermal pattern.

As can be seen in Fig. 1(b), the thermal pattern of each film changes its uniformity in the out-of-plane direction depending on the thickness of the film relative to the thermal penetration depth.²³ For instance, the $1 \mu m$ film shows a nonuniform thermal profile, where the high temperature spots penetrate only the top portion of the film. In contrast, the 0.25 μ m film in Fig. 1(d) shows a nearly uniform thermal profile with high and low temperature regions that are largely maintained throughout the thickness of the film. When observing the transient thermal behavior of the films, we see that the system is able to achieve steady state in a small amount of time, as can be seen in Fig. 2. The pattern reaches steady state within 3 ns, which is less than one-third of the period of the modulation. Because of this relatively small transient period, we ignore the transient thermal effects in our system. We suggest that the acoustic waves thermoelastically excited by the spatiotemporal modulation field will not be efficiently excited as their wavelength and frequency do not fall on the band diagram for these films. Furthermore, because linear elastic equations are used, any waves by the spatiotemporal modulation will not influence the nonreciprocal behavior of the film at the acoustic wave frequency of interest.

III. RESULTS AND DISCUSSION

A. Nonreciprocal band structure

We characterized the band structure of the spatiotemporally modulated systems as described previously. The point loads primarily excite the antisymmetric modes of the film. Out-of-plane displacements are measured along the top surface of the film at intervals of $0.2\,\mu\text{m}$. Two-dimensional (space and time) fast Fourier transforms (FFTs) were used to generate the band diagrams shown in Fig. 3.

The band diagram in Fig. 3(a) shows the band structures of primarily flexural modes of the 1 μ m thick film, as evident by the quadratic dispersion of the lowest-lying band in the first BZ.²⁶ The lack of a clear bandgap stems from the lack of modulation uniformity in the film depth. Figure 3(b) corresponds to the 0.5 μ m thick film, and the band diagram shows two distinct bandgaps centered approximately at 212 and 363 MHz for negative and positive wavevectors, respectively. Bands extending from the second BZs "L" and "R" in

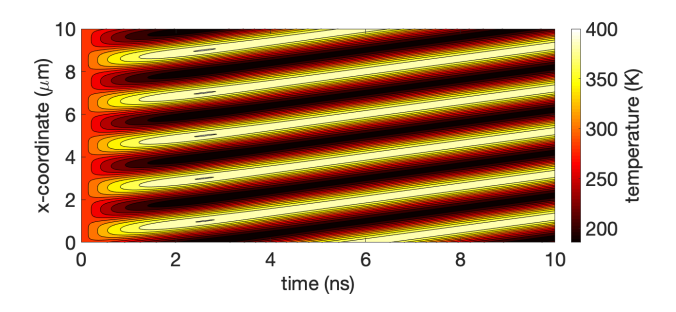


FIG. 2. (Color online) The transient thermal behavior of a $10\,\mu\mathrm{m}$ length region of the $0.5\,\mu\mathrm{m}$ thick film at a depth halfway through the film over a $10\,\mathrm{ns}$ period is depicted. The thermal pattern reaches steady state within 3 ns of being initiated.

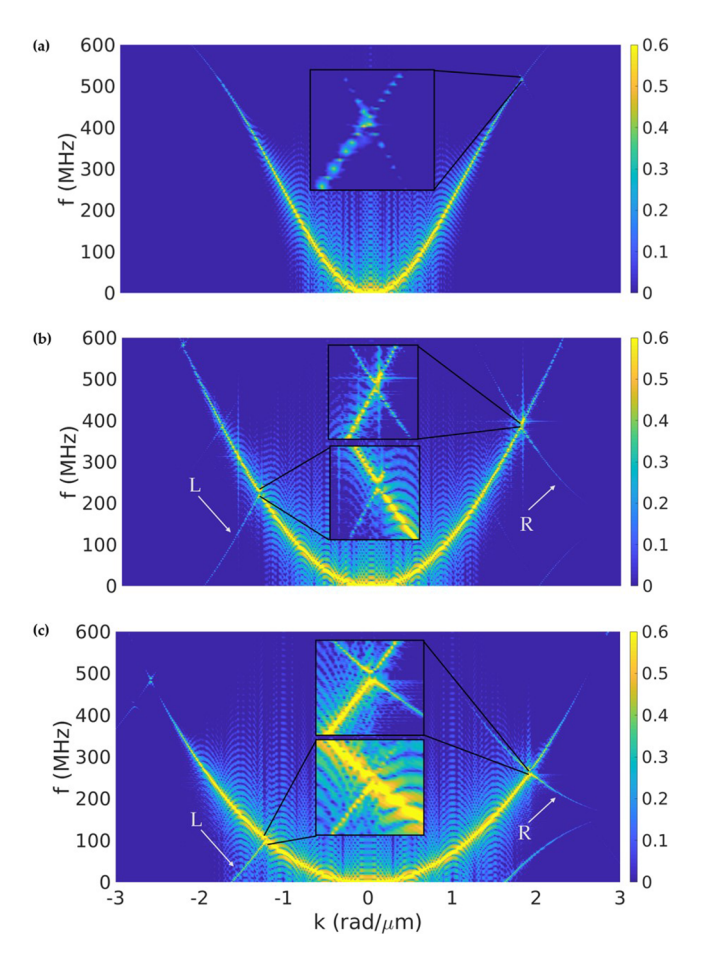


FIG. 3. (Color online) The 2D FFTs measured for films of (a) 1 μ m, (b) 0.5 μ m, and (c) 0.25 μ m thicknesses subjected to spatiotemporally periodic surface heating and an out-of-plane impulsive acoustic excitation, where f and k are the frequency and wavenumber of the propagating acoustic wave, respectively, are shown. The inset magnifies the band intersection induced by the spatiotemporal modulation. The color bar shows the amplitude of the FFT normalized by the maximum amplitude for each dispersion plot.

Fig. 3(b) are shifted $\pm 150\,\mathrm{MHz}$ (equal to the modulation frequency) relative to the primary band, and hybridization occurs where the bands intersect, resulting in asymmetric bandgaps. The band structure for the $0.25\,\mu\mathrm{m}$ thick film shown in Fig. 3(c) is similar to that shown for the $0.5\,\mu\mathrm{m}$ thick film but with wider bandgaps relative to their center frequency. The band diagram shows two distinct bandgaps centered at about 94 and 241 MHz for negative and positive wavevectors, respectively. It is determined that the penetration depth ratio, r_p , necessary to form asymmetric bandgaps is between 0.456 and 0.912 for this system.

B. Analytical model of partially modulated quasi-one-dimensional system

We now present an analytical model representing the modulation seen in the aluminum thin films to justify the presence and location of the bandgaps given the vertically inhomogeneous elastic property modulation field. The system is represented by two coupled elastic waveguides in which spatiotemporal modulation of stiffness is only applied to the top guide, as can be seen in Fig. 4(a), which models

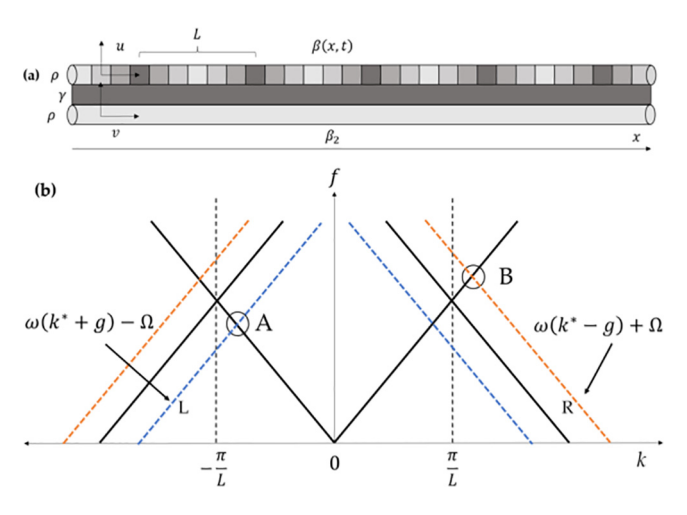


FIG. 4. (Color online) The (a) schematic of the analytical model describing coupled elastic waveguides and (b) schematic of the conditions required for resonance in the analytical system with $g=2\pi/L$ are depicted. The solid lines show primary bands $\omega(k^*)$, $\omega(k^*+K)$, and $\omega(k^*-K)$. The blue dashed line shows $\omega(k^*+g)-\Omega$, which intersects with $\omega(k^*+g-K)$ at point A. The orange dashed line shows $\omega(k^*-g)+\Omega$, which intersects with $\omega(k^*-g+K)$ at point B.

the behavior of a heated system with an r_p of 0.5. The equations of motion for the system are given as

$$\rho \frac{\partial^2 u}{\partial t^2} = \frac{\partial}{\partial x} \left(\beta(x, t) \frac{\partial u}{\partial x} \right) - \gamma(u - v),$$

$$\rho \frac{\partial^2 v}{\partial t^2} = \beta_2 \frac{\partial^2 v}{\partial x^2} + \gamma(u - v),$$
(1)

where ρ represents the mass density of each waveguide, u represents the displacement of the top guide, and v represents the displacement of the bottom guide. The term γ is the stiffness per unit volume and represents the coupling between waveguides. The bottom waveguide has constant elastic modulus, β_2 , whereas the top waveguide has spatiotemporally modulated modulus, $\beta(x,t)$, and they are modeled as

$$\beta(x,t) = \beta_0 + 2\beta_1 \sin(Kx - \Omega t), \tag{2}$$

where $K=2\pi/L$, where L is the spatial period of the modulation, and Ω is the angular frequency of modulation. We note that in the absence of modulation and coupling, the model of Eq. (1) does not capture the quadratic dispersion of flexural waves as shown in the simulation results and rather describes linear nondispersive waves for a single degree of freedom. We choose this as a first step to justify the presence and location of the asymmetric bandgaps in the presence of vertically inhomogenous material property modulation fields and suggest that future studies may augment this model to account for flexural mode dispersion. Along this line, a recent study also numerically explored asymmetric Lamb wave propagation enabled by spatiotemporal material property modulation.²⁷

We now choose Bloch waves as solutions to the system of Eq. (2),

$$u(x,t) = \sum_{k} \sum_{g} u(k,t)e^{-ikx},$$

$$v(x,t) = \sum_{k} \sum_{g} v(k,t)e^{-ikx},$$
 (3)

where $k = (k^* + g)$, $g = 2\pi m/L$ for $m \in \mathbb{Z}$, $k^* \in [-\pi/L, \pi/L]$ and $x \in [0, L]$. After substituting the solutions [Eq. (3)] into the system of Eq. (1), we obtain

$$\frac{\partial^2 u(k,t)}{\partial t^2} + \frac{\beta_0}{\rho} k^2 u(k,t) + \frac{\gamma}{\rho} (u(k,t) - v(k,t))$$

$$= i\epsilon f_1 u(k',t) e^{i\Omega t} + i\epsilon f_2 u(k'',t) e^{-i\Omega t}, \tag{4}$$

$$\frac{\partial^2 v(k,t)}{\partial t^2} + \frac{\beta_2}{\rho} k^2 v(k,t) - \frac{\gamma}{\rho} (u(k,t) - v(k,t)) = 0, \quad (5)$$

where $\epsilon = \beta_1/\rho$, $f_1 = -Kk' - (k')^2$ for k' = k - K and $f_2 = -Kk'' + (k'')^2$ for k'' = k + K. Note that Eq. (4) can be obtained by multiplying both sides of Eq. (1) by $e^{i\kappa x}$, where κ is a placeholder wavevector, integrating with respect to x from 0 to L and equating with the Dirac delta function. Multiple time scale perturbation theory was applied to second-order correction to analytically interpret the behavior of the quasi-one-dimensional (1D) system chain (see the Appendix). We show that there is a correction to the second-order to the band structure of the system,

$$\delta\omega(k) = \frac{-1}{2\omega_0} \left\{ \frac{f_1^2}{(\omega_0')^2 - (\omega_0 - \Omega)^2} + \frac{f_2^2}{(\omega_0'')^2 - (\omega_0 + \Omega)^2} \right\},\tag{6}$$

where ω_0 , ω'_0 , and ω''_0 denote the frequencies of the zerothorder dispersion relations for wavenumbers k, k', and k'', respectively, as is detailed in the Appendix. We see that the correction is large when the two denominators of each term in Eq. (6) approach zero. This gives rise to two resonance conditions for our system in which bandgaps will form

$$(\omega_0 - \Omega)^2 \sim (\omega_0')^2,$$

 $(\omega_0 + \Omega)^2 \sim (\omega_0'')^2.$ (7)

By plotting these conditions, we can visualize where the correction is large and where bandgaps will be opened due to the corrections, as is shown in Fig. 4(b).

Figure 4(b) shows where the conditions of Eq. (7) are satisfied, which indicates where bandgaps will form. The orange and blue curves in the second BZ are representative of the bands L and R shifted by the frequency, Ω , in Fig. 3. As can be seen, the intersections of these bands at points A and B are asymmetric with the bands at A crossing within the first BZ while the bands at B cross outside of the first BZ at a lower frequency. At these points, the correction to the dispersion relation will be high and bandgaps will form, causing the system to have an asymmetric band structure because of the asymmetry of where the bands at points A and B cross. This result agrees with the observation in

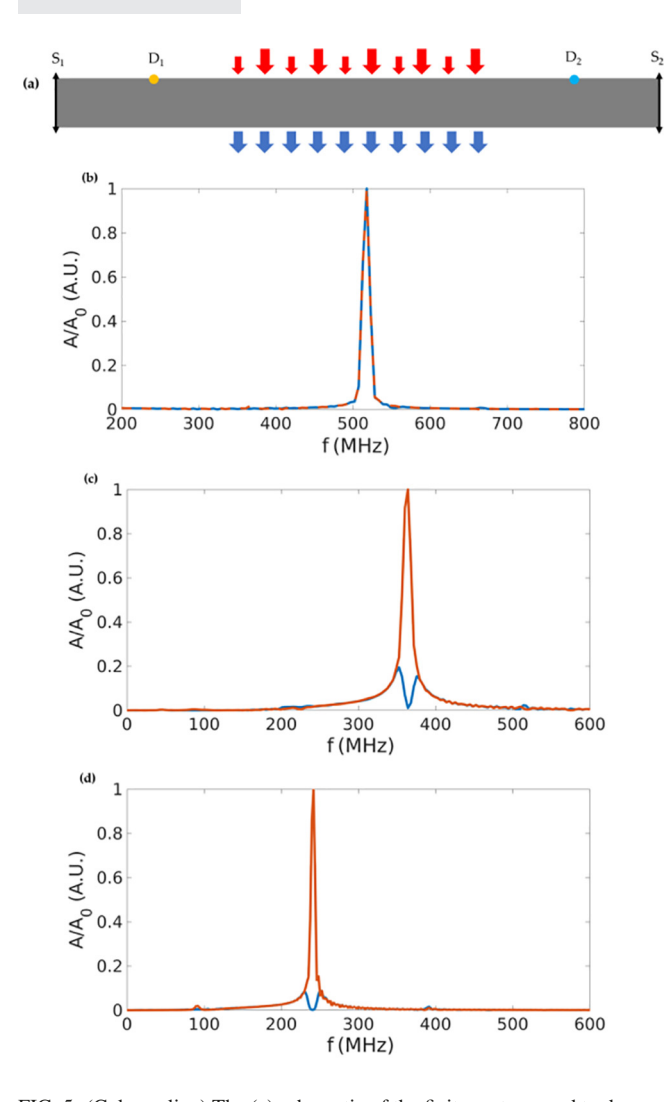


FIG. 5. (Color online) The (a) schematic of the finite system used to demonstrate nonreciprocal propagation with single frequency boundary driving is shown. Transmission spectra of (b) 1 μ m, (c) 0.5 μ m, and (d) 0.25 μ m thick finite phononic crystal excited at 517 MHz, 363 MHz, and 241 MHz, respectively, are depicted. The blue curve represents transmission for right propagating waves (positive wavevector). The orange curve represents transmission for left propagating waves (negative wavevector).

metallic thin films that uniform modulation throughout the depth of the system is not required for the system to break reciprocity and support nonreciprocal wave propagation. The analytical model demonstrates the effect of the modulation frequency, Ω , on the shift in the bandgap location, which is valid for all modulation speeds below the speed of sound in the film. Studies investigating the effect of modulation frequency on acoustic behavior have been conducted previously. ^{6,28}

C. Demonstration of nonreciprocal propagation

We now demonstrate nonreciprocal acoustic wave propagation using single frequency boundary excitation. The frequency of excitation, ω_{bg} , was chosen to lie within the bandgap frequency range of each of the films. As is shown in Fig. 5(a), the vertical displacement of the film was monitored at two locations, D_1 and D_2 , which were used to measure the amplitude of the transmitted wave after propagating through the phononic crystal. The transmission ratio of the films is independent of the depth of the locations of D_1 and D_2 . The transmission spectra were calculated by taking a FFT (with amplitude A) of the time domain signal and normalizing to the maximum of the input measurement position's spectrum (denoted by A_0). The simulation duration is 1000 ns. For Fig. 5(b), corresponding to the 1 μ m thick film with partial thermal penetration, the two spectra representing the right and left propagating waves lie nearly on top of each other at 517 MHz, which represents reciprocal wave propagation and complements the lack of clear bandgap formation shown in Fig. 3(a). Figure 5(c) represents the transmission spectra of the $0.5 \,\mu m$ finite phononic crystal film when excited near the bandgap center frequency at 363 MHz, and the spectrum is calculated using a 260 ns window following the wave that first reaches the detector point. Figure 5(d) similarly represents the transmission spectra for the $0.25 \,\mu m$ thick film when excited in the bandgap at a frequency of 241 MHz. Due to the wave velocity at this frequency, a larger 460 ns window of the incident signal is used for the spectral analysis. For the 0.5 and 0.25 μ m thick films, the left propagating wave spectra show largely unattenuated propagation, whereas the right propagating waves show a strong dip resulting from reflection in the bandgap frequency range. There are also two smaller peaks for each signal (for instance, at 213 MHz and 513 MHz for the $0.5 \,\mu \text{m}$ thick film), which are shifted by the modulation frequency away from the primary peak. Figure 6 shows the

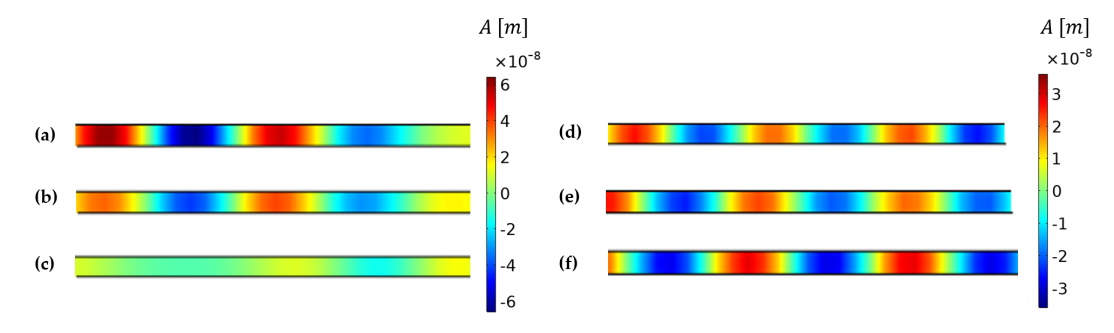


FIG. 6. (Color online) The out-of-plane displacement fields of waves at a bandgap frequency 363 MHz for 0.5 μ m film at 200 ns is depicted. The right-propagating waves show attenuation in amplitude from (a) $x \in [170, 180] \, \mu$ m, (b) $x \in [230, 240] \, \mu$ m, and (c) $x \in [290, 300] \, \mu$ m. The left-propagating waves show little to no attenuation from (d) $x \in [420, 430] \, \mu$ m, (e) $x \in [360, 370] \, \mu$ m, and (f) $x \in [300, 310] \, \mu$ m. The uniform displacement with depth is indicative of antisymmetric vibration modes.

out-of-plane component of the displacement fields of the 0.5 μ m film as waves at bandgap frequency (363 MHz) propagate to the right [Figs. 6(a)–6(c)] and to the left [Figs. 6(d)–6(f)]. As can be seen in Fig. 6, right-propagating waves have diminishing amplitude along the length of the film while left-propagating waves are sustained and maintain a similar amplitude as they propagate. The uniform displacement profile with the depth is characteristic of the antisymmetric vibration modes excited in the film.

IV. CONCLUSIONS

We have computationally demonstrated a strategy for enabling nonreciprocal acoustic wave propagation induced via thermoelastic spatiotemporal material property modulation. It was shown that nonreciprocal wave propagation could be further achieved, within limits, while the modulation is nonuniform and does not span the entire depth of the film. Future studies may involve the development of analytical models to better understand the effect of modulated pattern depth on quasi-1D phononic crystals, experimental demonstrations leveraging photo- or electrothermal modulation, and explorations of applications in signal processing devices.

ACKNOWLEDGMENTS

This research was funded by the National Science Foundation Emerging Frontiers in Research and Innovation (EFRI) Award No. EFMA-1640860, including multiple Research Experience and Mentoring (REM) supplements, which supported contributions by J.P., A.C., R.G., T.L., R.C., G.L.M., A.O., and N.S. J.A. acknowledges support from the Mechanical Engineering Department, King Fahd University of Petroleum and Minerals (KFUPM).

APPENDIX

Starting with the system of equations (4), we express the displacement in each of the waveguides as a second-order power series in the perturbations, ϵ , for cases where ϵ is assumed to be small

$$u(k,t) = u_0(k,\tau_0,\tau_1,\tau_2) + \epsilon u_1(k,\tau_0,\tau_1,\tau_2)$$

+ $\epsilon^2 u_2(k,\tau_0,\tau_1,\tau_2),$ (A1)

$$v(k,t) = v_0(k,\tau_0,\tau_1,\tau_2) + \epsilon v_1(k,\tau_0,\tau_1,\tau_2)$$

+ $\epsilon^2 v_2(k,\tau_0,\tau_1,\tau_2),$ (A2)

where u_i and v_i represent the displacement functions to the ith order. The time variables are replaced with $\tau_0 = t$, $\tau_1 = \epsilon t$, and $\tau_2 = \epsilon^2 t$, representing the multiple time scales. To the zeroth-order, the equations become

$$\frac{\partial^{2} u_{0}(k,\tau)}{\partial \tau_{0}^{2}} + \frac{\beta_{0}}{\rho} k^{2} u_{0}(k,\tau) + \frac{\gamma}{\rho} (u_{0}(k,\tau) - v_{0}(k,\tau)) = 0,$$
(A3)

$$\frac{\partial^2 v_0(k,\tau)}{\partial \tau_0^2} + \frac{\beta_2}{\rho} k^2 v_0(k,\tau) - \frac{\gamma}{\rho} (u_0(k,\tau) - v_0(k,\tau)) = 0,$$
(A4)

where τ is the compact notation for τ_0 , τ_1 , and τ_2 . Solutions to the zeroth-order equations take the form of a Bloch wave,

$$u_0(k, \tau_0, \tau_1, \tau_2) = a_0(k, \tau_1, \tau_2)e^{i\omega_0\tau_0},$$
 (A5)

$$v_0(k, \tau_0, \tau_1, \tau_2) = b_0(k, \tau_1, \tau_2) e^{i\omega_0 \tau_0}, \tag{A6}$$

where ω_0 is a function of k. Under the assumption that $\beta_0 = \beta_2$, the zeroth-order dispersion relation then becomes

$$\omega_0 = \sqrt{\frac{\beta_0}{\rho} k^2 + \frac{\gamma \pm \gamma}{\rho}},\tag{A7}$$

which represents the dispersion relation for propagation in a homogeneous medium. To eliminate secular terms that resonate with the frequency, ω_0 , the first-order equations assume that u_0 and v_0 are independent of τ_1 . The first-order equations are then given by

$$\frac{\partial^{2} u_{1}(k,\tau)}{\partial \tau_{0}^{2}} + \frac{\beta_{0}}{\rho} k^{2} u_{1}(k,\tau) + \frac{\gamma}{\rho} (u_{1}(k,\tau) - v_{1}(k,\tau))
= i f_{1} u_{0}(k',\tau) e^{i\Omega\tau_{0}} + i f_{2} u_{0}(k'',\tau) e^{-i\Omega\tau_{0}},$$
(A8)

$$\frac{\partial^2 v_1(k,\tau)}{\partial \tau_0^2} + \frac{\beta_0}{\rho} k^2 v_1(k,\tau) - \frac{\gamma}{\rho} (u_1(k,\tau) - v_1(k,\tau)) = 0.$$
(A9)

Solutions to Eqs. (A8) and (A9) can be represented as the combination of the homogeneous solution (which takes the form of the zeroth-order solution) and a particular solution. We seek particular solutions of the form

$$u_{1,p}(k,\tau) = Ae^{i(\omega_0' + \Omega)\tau_0} + Be^{i(\omega_0'' - \Omega)\tau_0},$$
 (A10)

$$v_{1,p}(k,\tau) = Ce^{i(\omega'_0 + \Omega)\tau_0} + De^{i(\omega''_0 - \Omega)\tau_0},$$
 (A11)

where ω_0 , ω'_0 , and ω''_0 denote ω_0 as a function of k, k', and k'', respectively. This allows us to solve for coefficients A, B, C, and D to find that

$$A = \frac{if_1 a_0(k', \tau_2)}{(\omega_0)^2 - (\omega_0' + \Omega)^2},$$
(A12)

$$B = \frac{if_2 a_0(k'', \tau_2)}{(\omega_0)^2 - (\omega_0'' + \Omega)^2},$$
(A13)

$$C = \frac{-\frac{\gamma}{\rho}if_1a_0(k', \tau_2)}{\left[(\omega_0)^2 - (\omega_0' + \Omega)^2\right]^2},$$
(A14)

$$D = \frac{-\frac{\gamma}{\rho} i f_2 a_0(k'', \tau_2)}{\left[(\omega_0)^2 - (\omega_0'' + \Omega)^2 \right]^2}.$$
 (A15)

For the second-order equations, we similarly assume that u_1 and v_1 are independent of τ_1 . The second-order equations are now given by

$$\begin{split} \frac{\partial^2 u_2(k,\tau)}{\partial t_0^2} + 2 \frac{\partial^2 u_0(k,\tau)}{\partial \tau_2 \partial \tau_0} + \frac{\beta_0}{\rho} k^2 u_2(k,\tau) + \frac{\gamma}{\rho} (u_2(k,\tau) \\ - v_2(k,\tau)) &= i f_1 u_1(k',\tau) e^{i\Omega \tau_0} + i f_2 u_1(k'',\tau) e^{-i\Omega \tau_0}, \end{split} \tag{A16}$$

$$\frac{\partial^2 v_2(k,\tau)}{\partial t_0^2} + 2 \frac{\partial^2 v_0(k,\tau)}{\partial \tau_2 \partial \tau_0} + \frac{\beta_0}{\rho} k^2 v_2(k,\tau)
- \frac{\gamma}{\rho} (u_2(k,\tau) - v_2(k,\tau)) = 0.$$
(A17)

There are terms that arise from the particular solution, $u_{1,p}(k,\tau)$, that take the form of $e^{i\omega_0\tau_0}$. These lead to secular behavior in the terms

$$F_{\text{secular}} = \left[if_1 B' + if_2 A'' \right] e^{i\omega_0 \tau_0}, \tag{A18}$$

where B' is a function of (k - K) and A'' is a function of (k + K). These two secular terms can be canceled by equating them to the second term in Eq. (A16),

$$2\frac{\partial^2 u_0(k,\tau)}{\partial \tau_2 \partial \tau_0} = \left[if_1 B' + if_2 A''\right] e^{i\omega_0 \tau_0}.$$
 (A19)

Equation (A19) will allow us to find the correction to the dispersion relation. Now that we have terms for $u_0(k,\tau)=a_0(k,\tau_2)e^{i\omega_0\tau_0}, \ A''=a(k'')a_0(k)$ in Eq. (A12), and $B'=b(k')a_0(k)$ in Eq. (A13), Eq. (A19) now takes the form

$$\frac{\partial a_0(k, \tau_2)}{\partial \tau_2} = \frac{1}{2\omega_0} \left[f_1 b(k') + f_2 a(k'') \right] a_0(k). \tag{A20}$$

We now choose solutions of the form $a_0(k,\tau_2)=a_0(k)e^{i\phi\tau_2}$, which makes $\partial a_0(k,\tau_2)/\partial \tau_2=a_0(k)i\phi e^{i\phi\tau_2}$. Substituting this derivative back into Eq. (A20) and solving for ϕ gives the expression for $\emptyset(k)=\delta\omega(k)$, which is the correction to the band structure appearing in Eq. (6) in the main text.

- ¹S. Harris and R. Wallace, "Acousto-optic tunable filter," J. Opt. Soc. Am. **59**(6), 744–747 (1969).
- ²Z. Yu and S. Fan, "Complete optical isolation created by indirect interband photonic transitions," Nat. Photonics **3**(2), 91–94 (2009).
- ³H. Lira, Z. Yu, S. Fan, and M. Lipson, "Electrically driven nonreciprocity induced by interband photonic transition on a silicon chip," Phys. Rev. Lett. **109**(3), 033901 (2012).
- ⁴M. Attarzadeh, J. Callanan, and M. Nouh, "Experimental observation of nonreciprocal waves in a resonant metamaterial beam," Phys. Rev. Appl. **13**(2), 021001 (2020).
- ⁵D.-W. Wang, H.-T. Zhou, M.-J. Guo, J.-X. Zhang, J. Evers, and S.-Y. Zhu, "Optical diode made from a moving photonic crystal," Phys. Rev. Lett. **110**(9), 093901 (2013).

- ⁶G. Trainiti and M. Ruzzene, "Non-reciprocal elastic wave propagation in spatiotemporal periodic structures," New J. Phys. 18(8), 083047 (2016).
- ⁷H. Nassar, H. Chen, A. Norris, and G. Huang, "Non-reciprocal flexural wave propagation in a modulated metabeam," Extreme Mech. Lett. **15**, 97–102 (2017).
- ⁸R. Verba, I. Lisenkov, I. Krivorotov, V. Tiberkevich, and A. Slavin, "Nonreciprocal surface acoustic waves in multilayers with magnetoelastic and interfacial Dzyaloshinskii-Moriya interactions," Phys. Rev. Appl. 9(6), 064014 (2018).
- ⁹Y. Wang, B. Yousefzadeh, H. Chen, H. Nassar, G. Huang, and C. Daraio, "Observation of nonreciprocal wave propagation in a dynamic phononic lattice," Phys. Rev. Lett. **121**(19), 194301 (2018).
- ¹⁰M. S. Kang, A. Butsch, and P. S. J. Russell, "Reconfigurable light-driven opto-acoustic isolators in photonic crystal fibre," Nat. Photonics 5(9), 549–553 (2011).
- ¹¹G. Trainiti, Y. Xia, J. Marconi, G. Cazzulani, A. Erturk, and M. Ruzzene, "Time-periodic stiffness modulation in elastic metamaterials for selective wave filtering: Theory and experiment," Phys. Rev. Lett. 122(12), 124301 (2019).
- ¹²H. Nassar, B. Yousefzadeh, R. Fleury, M. Ruzzene, A. Alù, C. Daraio, A. N. Norris, G. Huang, and M. R. Haberman, "Nonreciprocity in acoustic and elastic materials," Nat. Rev. Mater. 5(9), 667–685 (2020).
- ¹³A. Maznev, A. Every, and O. Wright, "Reciprocity in reflection and transmission: What is a 'phonon diode?,'" Wave Motion 50(4), 776–784 (2013).
- ¹⁴C. Shen, X. Zhu, J. Li, and S. A. Cummer, "Nonreciprocal acoustic transmission in space-time modulated coupled resonators," Phys. Rev. B 100(5), 054302 (2019).
- ¹⁵D. Torrent, O. Poncelet, and J.-C. Batsale, "Nonreciprocal thermal material by spatiotemporal modulation," Phys. Rev. Lett. **120**(12), 125501 (2018).
- ¹⁶J. A. Rogers and K. A. Nelson, "Study of Lamb acoustic waveguide modes in unsupported polyimide thin films using real-time impulsive stimulated thermal scattering," J. Appl. Phys. 75(3), 1534–1556 (1994).
- ¹⁷J. Laskar, S. Bagavathiappan, M. Sardar, T. Jayakumar, J. Philip, and B. Raj, "Measurement of thermal diffusivity of solids using infrared thermography," Mater. Lett. 62(17-18), 2740–2742 (2008).
- ¹⁸E. H. Buyco and F. E. Davis, "Specific heat of aluminum from zero to its melting temperature and beyond. Equation for representation of the specific heat of solids," J. Chem. Eng. Data 15(4), 518–523 (1970).
- ¹⁹J. Tallon and A. Wolfenden, "Temperature dependence of the elastic constants of aluminum," J. Phys. Chem. Solids 40(11), 831–837 (1979).
- ²⁰K. Davoudi, "Temperature dependence of the yield strength of aluminum thin films: Multiscale modeling approach," Scr. Mater. 131, 63–66 (2017).
- ²¹P. Foteinopoulos, A. Papacharalampopoulos, and P. Stavropoulos, "On thermal modeling of additive manufacturing processes," CIRP J. Manuf. Sci. Technol. 20, 66–83 (2018).
- ²²B. Burrows and D. Colwell, "The Fourier transform of the unit step function," Int. J. Math. Educ. Sci. Technol. 21(4), 629–635 (1990).
- ²³Y. K. Koh and D. G. Cahill, "Frequency dependence of the thermal conductivity of semiconductor alloys," Phys. Rev. B 76(7), 075207 (2007).
- ²⁴ASM Handbook, Properties and Selection: Nonferrous Alloys and Special-Purpose Materials (ASM International, Materials Park, OH, 1990), Vol. 2.
- ²⁵R. J. Richards, W. G. Steward, and R. B. Jacobs, "A survey of the literature on heat transfer from solid surfaces to cryogenic fluids," United States Department of Commerce, Office of Technical Services (1961).
- ²⁶H. Lamb, "On waves in an elastic plate," Proc. R. Soc. London, Ser. A 93(648), 114–128 (1917).
- ²⁷L. Zhao and C. Q. Lai, "Asymmetric Lamb wave propagation and mode isolation in thin plate with spatiotemporal periodic stiffness," ASME J. Vib. Acoust. 141, 051005 (2019).
- ²⁸C. Croënne, J. Vasseur, O. Bou Matar, M.-F. Ponge, P. Deymier, A.-C. Hladky-Hennion, and B. Dubus, "Brillouin scattering-like effect and non-reciprocal propagation of elastic waves due to spatio-temporal modulation of electrical boundary conditions in piezoelectric media," Appl. Phys. Lett. 110(6), 061901 (2017).